Pharmaceutical Sciences and Drug Design
ISSN: 3062-4428
2025, Volume 5, Issue 2, Page No: 186-203

Available online at: www.galaxypub.co/page/journals

Galaxy Publication

Galaxy Publication

Computational Discovery of Potential HDAC6 Inhibitors through Integrated Virtual Screening and Molecular Dynamics Approaches

Maria Gonzalez[1]*, Javier Ruiz[1], Lucia Torres[2], Elena Ruiz[1]

[1]Department of Drug Discovery and Pharmaceutical Chemistry, Faculty of Pharmacy, University of Granada, Granada, Spain.
[2]Department of Therapeutic Molecular Design, Faculty of Medicine, University of Seville, Seville, Spain.

***E-mail** ✉ maria.gonzalez@gmail.com

Received: 01 May 2026; **Revised:** 05 October 2026; **Accepted:** 11 October 2026

ABSTRACT

Histone deacetylase 6 has emerged as a significant therapeutic target due to its essential role in neurological, inflammatory, and other pathological conditions. At present, no HDAC6-targeting agents have received FDA approval, and most pipeline candidates exhibit limitations, including insufficient target occupancy, inadequate brain exposure, and poor tolerability. A small number of clinical-stage candidates exist, primarily for non-CNS malignancies. Yet, their pharmacokinetic drawbacks preclude application in neurological diseases associated with HDAC6, underscoring the necessity for new solutions that address these shortcomings. Moreover, these compounds display off-target toxicity attributable to limited selectivity, culminating in adverse reactions among patients. As a result, the emphasis of development over the last ten years has centered on selective inhibitors; nonetheless, no selective and potent HDAC6 inhibitor has yet received approval. The present investigation conducted an integrated virtual screening campaign against HDAC6 using the DrugBank database to identify existing drugs that could be repurposed to suppress HDAC6 activity. The initial assessment consisted of evaluating the binding capacity of molecular entities toward HDAC6. Thereafter, interaction profiling and 500 ns molecular dynamics simulations, combined with essential dynamics, were performed to probe the conformational adaptability and structural stability of HDAC6 upon binding to the identified compounds, specifically penfluridol and pimozide. The virtual screen highlighted penfluridol and pimozide as prospective repurposed therapeutic agents targeting HDAC6, a selection grounded in their binding potency and favorable drug-like characteristics. Docking analyses revealed that penfluridol and pimozide lodge within the same binding cleft on HDAC6 as the reference inhibitor. MD trajectories confirmed the establishment of stable protein–ligand assemblies between HDAC6 and both molecules. Complementary MMPBSA computations yielded favorable binding free energies across all HDAC6–ligand complexes, substantiating the stability of their interactions. Overall, the study indicates that both penfluridol and pimozide bind HDAC6 with strong, favorable interactions, lending credence to the notion of repurposing these agents to treat neurodegenerative disorders. That said, subsequent rigorous investigations remain necessary to delineate their effectiveness and safety profiles within biological settings.

Keywords: Histone deacetylase 6, Neurodegenerative diseases, Drug repurposing, Small-molecule inhibitors, Virtual screening

How to Cite This Article: Gonzalez M, Ruiz J, Torres L, Ruiz E, Computational Discovery of Potential HDAC6 Inhibitors through Integrated Virtual Screening and Molecular Dynamics Approaches. Pharm Sci Drug Des. 2025;5(2):186-203. https://doi.org/10.51847/n3qDRlSGRU

Introduction

Histone deacetylases constitute a family of enzymes that play a critical role in transcriptional control by altering histone epigenetic marks [1]. Beyond chromatin modification, select family members govern an array of cellular pathways by removing acetyl groups from non-histone substrates, including α-tubulin, ubiquitin, HSP90, cortactin, peroxiredoxins, and numerous transcription factors [2]. This family comprises 18 distinct members, divided into four classes based on sequence homology with yeast counterparts [3]. Class I encompasses HDAC1, 2, 3, and 8, which are classified based on their homology with the yeast Rpd3 protein [3]. These isoforms display

ubiquitous tissue distribution and participate in transcriptional regulation [4]. Class II HDACs, which share homology with yeast Hda1, possess the ability to traffic between the cytoplasmic and nuclear compartments and demonstrate tissue-restricted expression [5]. This class is further split into class IIa (HDAC4, 5, 7, and 9) and class IIb (HDAC6 and 10) [6]. The sole class IV enzyme, HDAC11, shows the greatest similarity to the catalytic domains of class I and II deacetylases [7]. Collectively, class I, II, and IV enzymes are designated as conventional HDACs, and all rely on Zn^{2+} as an essential cofactor. In contrast, class III HDACs, known as sirtuins (SIRT1–7), require NAD^{+} and are related to the yeast Sir2 protein. Through isoform-specific gene silencing and pharmacological inhibition, HDACs have been tied to diverse cellular functions [8]. Isoform-selective small-molecule inhibitors are projected to deliver superior efficacy alongside reduced toxicity for chronic treatment strategies in oncology and neurodegeneration [9]. Accordingly, significant resources have been dedicated to elucidating the specific roles of individual HDAC isoforms, paving the way for the rational design of selective HDAC inhibitors.

HDAC6, in particular, has drawn substantial research interest owing to its unique structural attributes [10]. The enzyme harbors two tandem N-terminal catalytic deacetylase domains, a C-terminal ZnF-UBP domain, and an SE14 tetradecapeptide repeat domain [11]. In addition, two leucine-rich nuclear export sequences facilitate its predominant cytosolic localization. HDAC6 deacetylates non-histone substrates, including α-tubulin, polyubiquitinated proteins, and HSP90, thereby influencing processes such as cell proliferation, motility, survival, protein turnover, and intracellular trafficking [12]. These activities are particularly significant for postmitotic cells, including neurons, which depend heavily on efficient protein quality control and axonal transport. Consequently, HDAC6 is under active investigation as a therapeutic node for malignancies as well as multiple neurodegenerative conditions, among them Alzheimer's disease, Parkinson's disease, Huntington's disease, and amyotrophic lateral sclerosis [13, 14].

Drug repurposing constitutes an efficient paradigm for generating novel therapies, effectively addressing the hurdles of high cost and protracted timelines inherent to de novo drug discovery [15]. This strategy capitalizes on pre-existing safety and pharmacokinetic datasets for FDA-approved medicines, opening the door to effective treatments for diseases beyond their originally intended indications [16]. In the realm of neurodegenerative disorders, where therapeutic options remain scarce and often suboptimal, repurposing presents a particularly attractive pathway toward new interventions. Current HDAC6-directed agents suffer from liabilities, including limited blood–brain barrier permeability and inadequate target selectivity [17]. Hence, via a drug repositioning framework, we seek to identify molecular entities that potently engage HDAC6 while circumventing these constraints, potentially yielding innovative treatment strategies for neurodegenerative diseases.

In this work, we focused on the HDAC6 protein to perform structure-guided drug repurposing. We therefore designed a multi-step screening funnel, commencing with molecular docking to pinpoint drug molecules best suited for productive interaction with HDAC6. Such computational approaches offer considerable value in both de novo drug discovery and repositioning, as they are markedly more economical and time-efficient than conventional experimental pipelines. A curated collection of 3500 FDA-approved drug entries was retrieved from the DrugBank repository [18]. The leading candidates were selected based on binding affinity and key molecular interactions with HDAC6. These shortlisted molecules underwent further evaluation of their drug-like attributes, and their docked configurations with HDAC6 were subjected to detailed atomic-scale examination through molecular dynamics simulations complemented by essential dynamics methodologies.

Materials and Methods

Molecular docking screening protocol

To spearhead a structure-informed virtual screening workflow, a strategy rooted in molecular docking was adopted to sieve molecules that bind tightly to HDAC6. The computational pipeline integrated MGL AutoDock tools [19], InstaDock 1.2 [20], PyMOL 3.1 [21], and Discovery Studio Visualizer 2023 [22], along with several internet-based analytical resources. The experimentally resolved three-dimensional structural model of HDAC6 was sourced from the Protein Data Bank under the identifier 5EDU, chain B, and prepared for docking experiments using InstaDock v1.2 and the AutoDock utility suite. Preparatory modifications to the structure entailed the remediation of missing loop segments, protonation of polar atoms, and the systematic assignment of appropriate atom types. The compound collection was procured from the DrugBank repository and formatted for virtual screening within InstaDock v1.2. The docking runs were executed within a blind sampling volume defined

by a rectangular grid with dimensions 65 Å × 77 Å × 63 Å, positioned so that its geometric center lay at 15.135 Å, −33.815 Å, and 92.124 Å along the X, Y, and Z Cartesian directions, respectively. A grid point separation of 1 Å was imposed, and the sampling box enveloped all non-hydrogen atoms of the receptor. This spatial window was deliberately oversized to encapsulate the full protein architecture, granting each ligand unrestricted translational and rotational freedom to canvas plausible binding sites. Once the docking sweep concluded, the entire compound collection was ranked by predicted binding affinity, and the highest-scoring molecular entities were earmarked for deeper scrutiny.

Biological capability and interaction study

The putative biological activity spectrum of the triaged molecules was predicted using the PASS web-based prediction engine, which juxtaposes the molecular framework of a query ligand against a reference library of documented biological activities [23]. The server infers activity profiles by decoding structure–activity relationships and expresses its predictions as paired 'probability to be active' (Pa) and 'probability to be inactive' (Pi) scores. A comparatively elevated Pa figure signals a greater prospect that the compound in question will exhibit the projected bioactivity. After the PASS profiling step, the binding architectures and contact networks of the high-priority compounds were explored. The intermolecular interfaces established between the candidate drugs and HDAC6 were inspected and rendered using PyMOL 3.1. Complementarily, Discovery Studio Visualizer was used to perform a meticulous breakdown of the interaction repertoire that may materialize within the confines of the HDAC6 active site. Only those compounds observed to tether with functionally indispensable residues—most notably active-site anchors such as His611—were promoted to the subsequent phase of evaluation.

MD simulations protocol

All-atom molecular dynamics simulations were performed to investigate, at the atomic level, how the binding dynamics of the HDAC6–drug assemblies evolve [24]. The simulations were run at pH 7.0, using the CHARMM36-jul2022 force field parameter set [25] in conjunction with the TIP3P explicit water model [26], all orchestrated within the GROMACS computational framework [27]. The addition of 12,580 water molecules accomplished solvation of each system. Topology parameter files for the three compounds under investigation—penfluridol, pimozide, and trichostatin A—were constructed with the assistance of the CGenFF online server [28]. The solvated systems were enclosed within a cubic periodic cell, ensuring a minimum separation of 10 Å between any protein atom and the container faces (resulting in box edge lengths of 8.41 × 8.41 × 8.41 nm in the x, y, and z directions). Eight Na^+ ions were introduced as neutralizing counterions to offset the net charge. Steric clashes and unfavorable contacts were alleviated through energy minimization using the steepest descent protocol, with 5000 steps and a tolerance cutoff of 10.0 kJ/mol. Following minimization, two sequential equilibration procedures were undertaken: first, sampling under an NVT ensemble, and second, under an NPT ensemble, each spanning 1000 ps. During these phases, the conserved state variables were the particle count, system volume, and temperature for the NVT step, and the particle count, system pressure, and temperature for the NPT step. The system temperature was held at 300 K throughout the NVT stage using the Berendsen thermostat with a coupling time constant of 0.1 ps.

In contrast, pressure regulation during the subsequent NPT stage was achieved with the Parrinello–Rahman barostat targeting a reference pressure of 1 bar with a coupling constant of 2.0 ps. Long-range electrostatic forces were handled using the particle-mesh Ewald summation technique, with Coulombic interactions truncated at 12 Å. A spherical cutoff of 1.0 nm was applied to van der Waals interactions. Trajectory propagation employed the leapfrog integration scheme with a time step of 2 fs, and covalent hydrogen bonds were constrained using the LINCS algorithm. Temperature coupling was maintained using the Berendsen approach, whereas pressure coupling during NPT equilibration used the Parrinello–Rahman method. The ultimate production phase extended over 500 ns, during which energy statistics and log outputs were captured every 10 ps. The resultant trajectory files were subsequently post-processed and interpreted using the analysis utilities integrated within the GROMACS suite. The temporal evolution of secondary structural elements was characterized using the DSSP classification algorithm [29].

Principal component analysis protocol

Principal component analysis was undertaken to isolate the essential dynamical characteristics of HDAC6 and its complexed forms, providing insight into the principal motional modes that govern protein stability and pliability

in response to ligand docking. This dimensionality-reduction methodology filters out inconsequential fluctuations to focus on strongly correlated atomic displacements that are functionally meaningful for conformational transitions [30]. The underlying covariance matrix was assembled from a concatenated compilation of atomic coordinate trajectories that collectively represent all simulated conditions of HDAC6—emphasizing the apo state and the three ligand-bound configurations. Embracing such a merged-trajectory framework permits an encompassing depiction of the protein's conformational behavior across disparate binding milieus, facilitating a rigorous dissection of the dynamic perturbations uniquely attributable to each ligand. The covariance matrix quantifies the variance and paired covariance among atomic coordinate vectors and is formally given by:

$$C_{ij} = \langle (x_i - \langle x_i \rangle)(x_j - \langle x_j \rangle) \rangle \quad (1)$$

Where xi and xj correspond to the positional coordinates of the i-th and j-th atoms in the system, and ⟨xi⟩ and ⟨xj⟩ designate their respective ensemble-averaged positions. Diagonalization of this covariance matrix yields the principal component eigenvectors.

The interpretative focus was on the two principal components, which together capture the dominant share of the overall positional variance. These leading components enabled delineation of prominent structural modifications induced by ligand binding, with particular scrutiny of inherently flexible stretches, such as loop motifs proximal to the binding site.

Free energy landscape generation

Construction of free energy landscapes furnishes a vivid depiction of the stability attributes and conformational interconversion pathways inherent to biomolecular systems, encompassing proteins and protein–ligand conjugates alike [31]. Delineation of the FEL helps identify stable configurational states and characterize the transition corridors that connect them. The free energy landscape is mathematically constructible through the relationship:

$$\Delta G(X) = -k_B T \ln P(X) \quad (2)$$

Where ΔG(X) symbolizes the free energy expressed as a function of the chosen reaction coordinate, kB is the Boltzmann constant, T represents the absolute temperature, and P(X) corresponds to the probability density of the conformational ensemble when projected onto the principal component subspace.

MMPBSA calculation

The molecular mechanics/Poisson–Boltzmann surface area approach is a widely used computational method for approximating binding free energies in protein–ligand systems [32]. In the current assessment, a condensed 10 ns window—covering the trajectory stretch from the 250 ns mark through to 260 ns—was carved out from the well-equilibrated, steady-state segments of the production runs belonging to the HDAC6–Penfluridol, HDAC6–Pimozide, and the reference HDAC6–Trichostatin A assemblies. Using the gmx_MMPBSA toolkit, the individual energetic contributions underlying the binding event were deconstructed and quantified. The overall binding free energy was arrived at through the relationship:

$$\Delta G_{\text{Binding}} = G_{\text{Complex}} - \left(G_{\text{Protein}} + G_{\text{Ligand}}\right) \quad (3)$$

Where GComplex captures the total free energy of the bound state, and GProtein together with GLigand represent the isolated total free energies of the HDAC6 receptor and each of the three small-molecule partners—penfluridol, pimozide, and trichostatin A—in turn.

Results and Discussion

Molecular docking screening

Molecular docking is a widely used computational method for predicting the most energetically favorable orientation and three-dimensional arrangement of a ligand upon binding to a protein receptor's binding cavity [33]. In the present investigation, an assembled library of 3500 FDA-sanctioned drug molecules was procured from the DrugBank database and subjected to docking-based screening. This screening campaign was conducted

with InstaDock to identify compounds with elevated binding affinity for HDAC6. The reliability of the adopted docking protocol was substantiated by redocking the co-crystallized ligand, trichostatin A, into the HDAC6 active pocket. Superimposition of the computationally generated binding poses with the experimentally resolved co-crystallized conformation demonstrated strong congruence, thereby affirming the procedural accuracy of the docking method. The close correspondence between the docked orientations and the crystallographic pose underscores the meticulousness of the protocol. This calibration step reinforces the trustworthiness of the docking framework and its prospective value in subsequent molecular docking endeavors. The overall procedure entailed assigning scores to every compound in the library, after which the 10 top-ranked entities were retained based on their docking scores against HDAC6, as listed in **Table 1.** The recorded scores, spanning −9.3 to −10.5 kcal/mol, serve as indicators of the interaction strength each ligand establishes with the receptor HDAC6. It is well appreciated that increasingly negative docking scores reflect progressively tighter binding affinities. Notably, all shortlisted molecules outperformed the reference co-crystallized inhibitor trichostatin A, which yielded a docking score of −6.6 kcal/mol (PDB IDs: 5EDU, TSN). In our docking experiments, the catalytic zinc ion was excluded by default per the InstaDock parameter settings. Considering the pivotal role that the zinc ion fulfills within the HDAC6 catalytic center—especially for inhibitors like trichostatin A that rely on a hydroxamate warhead to chelate the metal ion—its deliberate absence may plausibly account for the comparatively weaker binding affinity registered during our docking calculations.

Table 1. List of screened hits against HDAC6 and their docking parameters.

S. No.	Drug	Torsional energy	Ligand efficiency (kcal/mol/non-H atom)	pKi	Binding affinity (kcal/mol)
1	Dutasteride	1.2452	0.2838	7.70	−10.5
2	Bisdequalinium Chloride	0	0.2318	7.48	−10.2
3	Conivaptan	1.2452	0.2632	7.33	−10.0
4	Penfluridol	2.8017	0.2778	7.33	−10.0
5	Pimozide	2.1791	0.2882	7.19	−9.8
6	Rolapitant	2.1791	0.2771	7.11	−9.7
7	Lumacaftor	1.8678	0.2848	6.89	−9.4
8	Difenoxin	2.4904	0.2938	6.89	−9.4
9	Phenindamine	0.3113	0.4650	6.82	−9.3
10	Acrivastine	2.1791	0.3577	6.82	−9.3
11	Trichostatin A	2.1791	0.3000	4.84	−6.6

To obtain a more nuanced characterization of the binding interactions, a set of complementary descriptors was evaluated, encompassing pKi, ligand efficiency, and torsional energy. The pKi metric translates docking-derived scores into a quantitative measure of binding potency between the ligand and its macromolecular target. Larger pKi values indicate increasingly robust predicted binding affinities, thereby offering a window into a compound's prospective inhibitory capability. Ligand efficiency is derived by normalizing the binding affinity relative to molecular bulk, expressed as the total number of non-hydrogen atoms in the molecule. This normalization permits a balanced appraisal of binding affinity disparities while concurrently accounting for molecular dimensions, enabling discrimination between ligands that are at once potent and structurally economical in their binding interactions. Torsional energy quantifies the energetic penalty associated with rotations around rotatable single bonds within the ligand scaffold. A lower torsional energy generally signals reduced intramolecular strain, suggesting that the ligand can adopt a more conformationally relaxed and stable pose once accommodated within the receptor pocket. This energetic parameter can significantly affect both the binding specificity and the long-term stability of the resultant protein–ligand binary assembly. Taken together, these indices provide a richer, more holistic depiction of the binding attributes of each molecular candidate. Drawing on the accumulated docking data, it can be concluded that the identified molecular hits are highly satisfactory in terms of their binding energetics and associated properties, providing ample justification for continued exploration and chemical optimization of these compounds as prospective HDAC6 inhibitors.

PASS analysis and drug profiling

The PASS computational server was used to predict the biological activity spectra of the molecules identified in the preceding docking-based screening stage [19]. In this study, PASS analysis was used to assess the biological

activity profiles of the highest-ranked candidates. Among the 10 molecules identified during the docking screen, a pair of compounds—specifically penfluridol and pimozide—stood out as particularly promising candidates upon drug profiling for the sought-after biological activities **(Table 2).** The PASS evaluation was carried out to probe the putative bioactivities of penfluridol, pimozide, and trichostatin A. Given that these compounds are well-characterized, extensively documented drugs, the bioactivity predictions from the PASS platform are anticipated and largely consistent with their recognized therapeutic functions. Nonetheless, the PASS tool further highlights supplementary prospective activities for these agents that extend beyond their firmly established therapeutic niches, furnishing an expanded perspective on their potential pharmacological effects. The PASS-generated readout pinpointed properties linked to the management of acute neurological conditions, alongside analgesic, anxiolytic, antipsychotic, and anti-migraine attributes, collectively underscoring that these molecular entities exhibit a pronounced capacity to address neurodegenerative disorders. The underlying principle holds that when the computed probability of a compound manifesting a given biological activity exceeds the probability of it remaining inactive (Pa > Pi), the likelihood of genuine bioactivity is considered substantial. Among the examined drugs, penfluridol and pimozide yielded the highest Pa values, ranging from 0.426 to 0.786, a spread indicative of considerable therapeutic potential for the management of neurological disturbances. The aggregate output of the PASS investigation pinpointed penfluridol and pimozide as the two molecular entities carrying the most propitious ensemble of biological activities when viewed through the lens of drug repurposing aimed squarely at HDAC6.

Table 2. PASS properties of the elucidated molecules with their predicted activity.

S. No.	Compound	Pi	Pa	Predicted biological activity
1	Penfluridol	0.010	0.786	Treatment of acute neurological disorders
		0.007	0.748	Pain-relieving (analgesic) effect
		0.005	0.586	Management of neurogenic pain
		0.094	0.662	Therapy for phobic disorders
		0.080	0.576	Anti-neurotic activity
2	Pimozide	0.011	0.610	Antipsychotic effect
		0.064	0.534	Treatment of acute neurological disorders
		0.011	0.475	Relief of neurogenic pain
		0.005	0.462	Anti-migraine activity
		0.056	0.426	Management of neurodegenerative diseases
3	Trichostatin A	0.002	0.765	Histone deacetylase inhibitory activity
		0.002	0.738	HDAC6 (histone deacetylase 6) inhibition
		0.002	0.734	Inhibition of class IIb HDAC enzymes
		0.002	0.693	Inhibition of class II HDAC enzymes
		0.035	0.533	Apoptosis-inducing (agonist) activity

Interaction analysis

Repositioning established pharmaceuticals toward alternative protein targets requires a thorough examination of the intermolecular interactions within the resulting protein–ligand assemblies, ensuring the desired biological response is achieved while minimizing spurious binding events [34]. In the present study, the binding topologies and residue-level contacts adopted by the repurposed candidates, penfluridol and pimozide, were systematically characterized, together with the benchmark ligand trichostatin A, using PyMOL in conjunction with Discovery Studio Visualizer **(Figure 1).** The ensemble of docking solutions yielded 27 conformational variants for each compound when bound to HDAC6, thereby providing a richer depiction of their respective interaction landscapes **(Figure 1a).** Both penfluridol and pimozide established multiple noteworthy contacts and assumed the most energetically preferred poses within the substrate-binding hollow of HDAC6, mirroring the behavior exhibited by trichostatin A **(Figure 1b)**. The two compounds, penfluridol and pimozide, lodged themselves inside the catalytic chamber of HDAC6; nevertheless, the spatial disposition of penfluridol departed markedly from that adopted by the reference agent trichostatin A **(Figure 1c)**. These findings collectively suggest that penfluridol and pimozide could hold considerable promise for exploitation as HDAC6-targeting inhibitors amenable to further medicinal chemistry refinement. It must be emphasized, however, that subsequent experimental verification is indispensable to conclusively establish the precise mode of inhibition and the therapeutic value of penfluridol and pimozide when acting upon HDAC6.

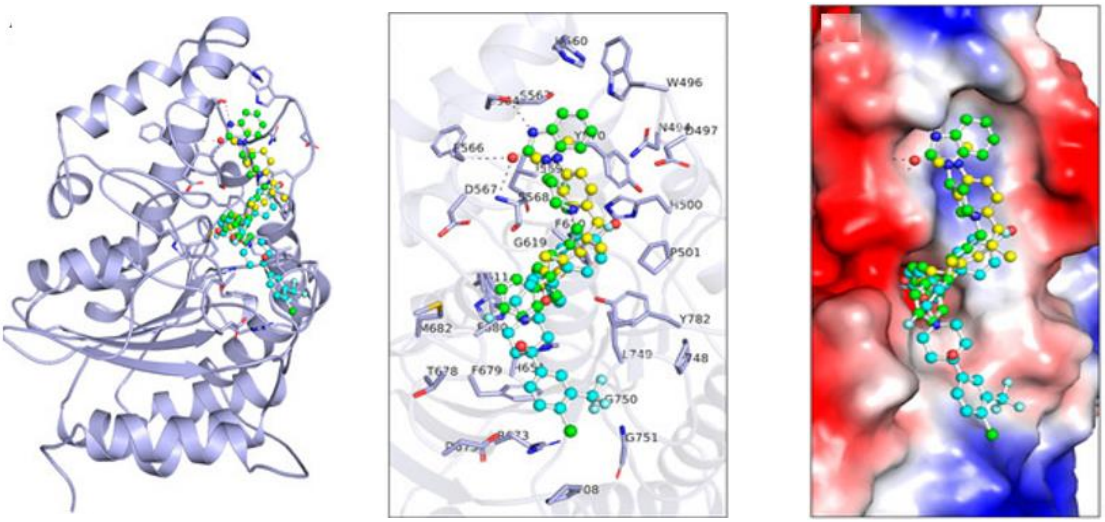

a) b) c)

Figure 1. Interaction pattern of selected molecules with HDAC6: (a) Binding pattern of HDAC6 with Penfluridol (cyan), Pimozide (green), and Trichostatin A (yellow), (b) Magnified view of HDAC6 binding pocket residues interacting with the binding pattern of HDAC6 with Penfluridol, Pimozide, and Trichostatin A, and (c) Surface potential view of HDAC6 with the selected drug molecules.

Extending the analysis to a finer level of granularity, the Discovery Studio Visualizer package was employed to conduct an exhaustive dissection of the formed contacts **(Figure 2)**. Penfluridol displayed an array of contact categories with HDAC6, including hydrogen bonds contributed by His611 and Arg673, halogen (fluorine) bonds furnished by Gly619, Leu749, and Gly750, alkyl-type contacts engaging Pro501, Phe679, Phe680, and Pro708, pi–pi T-shaped together with amide–pi stacked geometries mediated by Phe620, His651, and Phe680, and a collection of van der Waals contacts enlisting His500, Ser568, Pro748, Gly751, and Tyr782 **(Figure 2a)**. In parallel, pimozide partook in an assortment of close-range contacts with HDAC6, most notably hydrogen bonds linking His500 and Ser568, halogen (fluorine) bonds with Gly619 and Thr678, a pi–anion pairing with Met682, an alkyl contact mediated by Phe620, pi–pi T-shaped and amide–pi stacked frameworks involving Phe620, His651, and Phe680, and a broad sweep of van der Waals contacts spanning Asn494, Trp496, Asp497, Pro501, His560, Ser563, Ser564, Phe566, Ile569, Tyr570, His611, Phe679, Leu749, and Tyr782 **(Figure 2b)**. Following a comparable pattern, the co-crystallized reference inhibitor trichostatin A engaged HDAC6 through hydrogen bonds connecting His610, Asp649, and Tyr782, pi–sigma contacts originating from Phe620 and Phe680, alkyl contacts supplied by His500, Pro501, Phe680, and Leu749, together with van der Waals contacts encompassing His499, Ser568, His611, Gly619, His651, Asp742, Gly780, and Gly781 **(Figure 2c)**. Among all cataloged interactions, penfluridol uniquely formed a hydrogen bond with the catalytic pocket residue His611. In contrast, pimozide and trichostatin A instead engaged this functionally indispensable residue solely through van der Waals forces. These structural insights furnish a compelling rationale for subjecting the identified compounds to subsequent molecular dynamics simulations, designed to unravel the temporal progression of their binding mechanisms and the conformational robustness they maintain in complex with HDAC6.

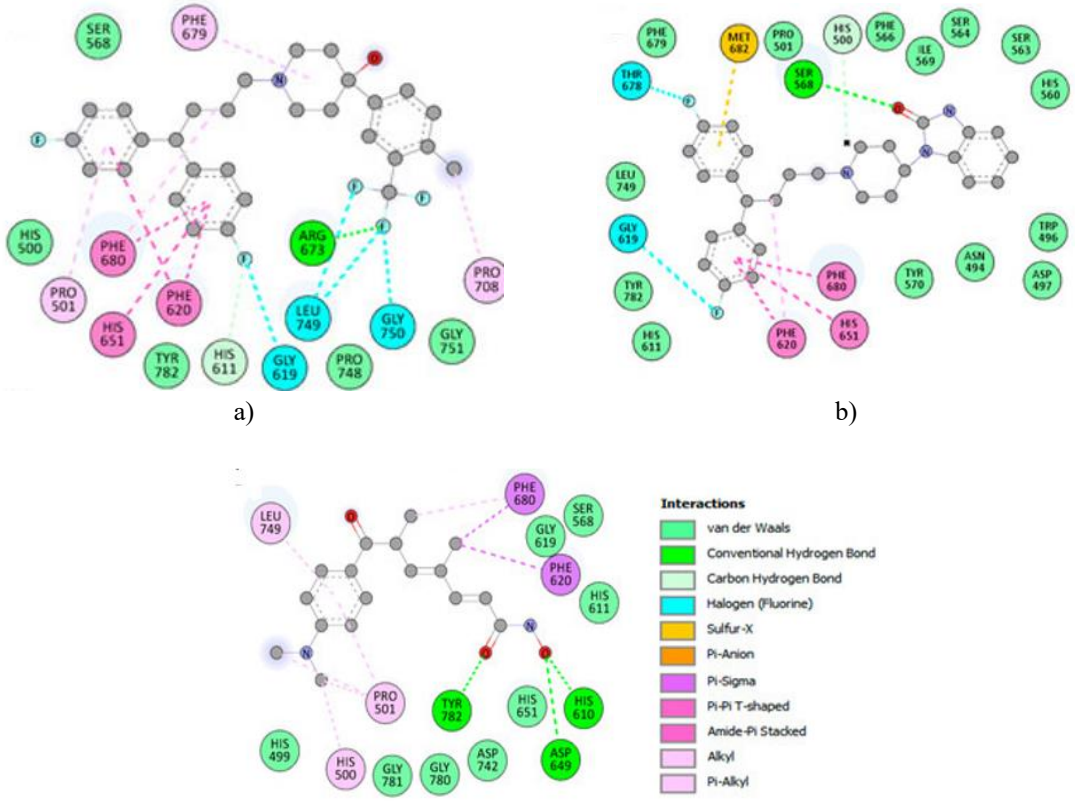

Figure 2. Binding residues of HDAC6 and their interactions with (a) Penfluridol, (b) Pimozide, and (c) Trichostatin A. Hydrogen atoms from the hydroxyl group (OH) are hidden for clarity.

MD simulations

Molecular dynamics simulation is a central and indispensable tool in molecular modeling and computer-aided design, enabling the interrogation of dynamical behavior and the time-resolved evolution of molecular architectures [35]. Within the scope of this work, four molecular ensembles were scrutinized: one apo HDAC6 entity and three HDAC6–drug binary assemblies. Before evaluating metrics such as deviation, fluctuation, and compactness across the systems, both potential and kinetic energy contributions were quantified to assess the foundational stability of each setup. The average potential energy values computed for apo HDAC6 and for the HDAC6–Penfluridol, HDAC6–Pimozide, and HDAC6–Trichostatin A complexes were −799,096 kJ/mol, −552,096 kJ/mol, −552,388 kJ/mol, and −551,954 kJ/mol, respectively. The counterpart mean kinetic energy values for apo HDAC6 and the HDAC6–Penfluridol, HDAC6–Pimozide, and HDAC6–Trichostatin A complexes were 155,797 kJ/mol, 111,168 kJ/mol, 111,173 kJ/mol, and 111,089 kJ/mol, respectively. While the kinetic energy component of every HDAC6–drug complex declined relative to the unliganded HDAC6 protein, the potential energy component concurrently shifted to more markedly negative magnitudes. This accentuation of negative potential energy indicates the formation of increasingly stable, energetically favorable contacts between the macromolecule and the docked ligands. A more negative potential energy reading is interpretable as a signature of a more highly stabilized assembly, given that the drug-bound states manifest reinforced intermolecular interactions that cooperatively lower the system's energetic landscape. Accordingly, the simultaneous drop in kinetic energy, paired with the deepening of negative potential energy, faithfully mirrors the stabilization of the HDAC6–drug complexes relative to the free HDAC6 protein.

Structural deviation analysis

The root-mean-square deviation (RMSD) metric provides a robust statistical measure of structural drift within molecular configurations [36]. Throughout the 500 ns MD production run, RMSD values were tracked to assess the overall conformational stability of each protein–ligand ensemble. By calculating RMSD across the entire complex, one can assess the occurrence of significant conformational shifts and determine whether the assembly maintains its integrity over the simulated timescale. Average RMSD values were compiled across all systems to

determine the magnitude of the HDAC6 structural perturbation following ligand association. As summarized in **Table 3**, the mean RMSD values attributed to apo HDAC6, the HDAC6–Penfluridol pair, the HDAC6–Pimozide pair, and the HDAC6–Trichostatin A pair stood at 0.24 nm, 0.24 nm, 0.27 nm, and 0.22 nm, respectively. The unbound HDAC6 protein and its penfluridol-bound counterpart yielded closely matched average RMSD values; the pimozide-bound system registered a slight uptick in RMSD, whereas the trichostatin A-bound complex returned the lowest average RMSD among the set. To supplement these averages, the peak RMSD for each system was also identified, capturing the most extreme deviation **(Figure 3a)**. Both the ligand-free HDAC6 and the penfluridol-associated complex reached an identical maximum RMSD of 0.33 nm. The pimozide-complexed form peaked at a somewhat elevated 0.36 nm, whereas the trichostatin A-bound assembly capped at 0.31 nm over the entire trajectory. Consistent with the main RMSD graph and its related frequency histogram, the HDAC6–Pimozide complex (illustrated in green) sustains a marginally higher RMSD envelope throughout the simulation course **(Figure 3a)**, (upper panel). The probability density function derived from RMSD values clusters predominantly within the 0.2–0.3 nm bracket **(Figure 3a),** (lower panel). Across the entire deviation dataset, all three liganded states exhibit progressively increasing stability as the 500 ns simulation progresses.

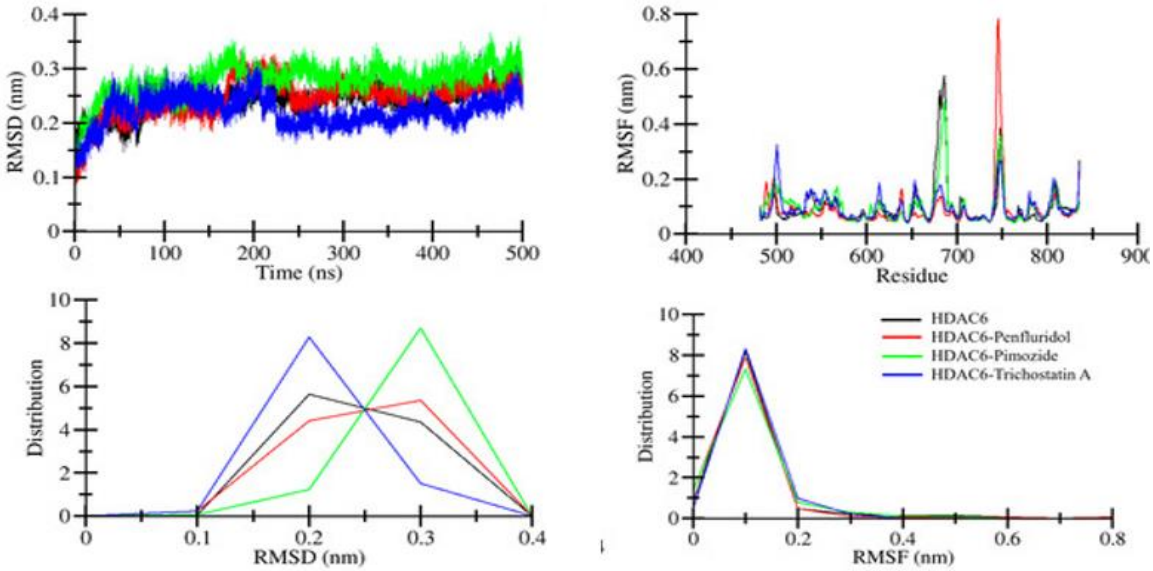

a) b)

Figure 3. Time-evolution dynamics of HDAC6: (a) Structural deviation analysis plot of RMSD of HDAC6, HDAC6-Penfluridol, HDAC6-Pimozide, and HDAC6-Trichostatin A, and (b) Residual fluctuation analysis plot of RMSF of HDAC6, HDAC6-Penfluridol, HDAC6-Pimozide, and HDAC6-Trichostatin A. The lower panels show the distributions of RMSD and RMSF for the PDFs.

Table 3. Average values calculated post 500 ns MD simulations of HDAC6 protein and HDAC6–drug complexes.

S. No.	System	Intramolecular H-bonds	SASA (nm²)	Radius of gyration (Rg, nm)	RMSF (nm)	RMSD (nm)
1	HDAC6	264 (± 8)	153.3 (± 3.42)	1.98 (± 0.01)	0.09 (± 0.08)	0.24 (± 0.03)
2	HDAC6–Penfluridol	264 (± 8)	150.5 (± 2.98)	1.98 (± 0.01)	0.08 (± 0.08)	0.24 (± 0.03)
3	HDAC6–Pimozide	267 (± 9)	156.2 (± 3.98)	2.00 (± 0.01)	0.10 (± 0.07)	0.27 (± 0.03)
4	HDAC6–Trichostatin A	264 (± 8)	150.8 (± 3.26)	1.98 (± 0.01)	0.09 (± 0.05)	0.22 (± 0.03)

Root-mean-square fluctuation (RMSF) provides an equally informative lens for assessing residue-specific motional freedom across simulated biomolecular architectures. RMSF analysis was applied to dissect how individual amino acid positions within the polypeptide chain vary in their conformational liberty. Positions with elevated RMSF values indicate protein regions with enhanced dynamic behavior, often associated with surface-exposed loops or inherently flexible modules. Such motional signatures can spotlight locales undergoing adaptive conformational remodeling in response to ligand docking, yielding a window into the protein's dynamic repertoire—the global mean RMSF was computed to capture the overall residue-scale mobility across all

simulated conditions. The average RMSF readings determined for apo HDAC6 alongside its penfluridol-, pimozide-, and trichostatin A-bound forms were 0.09 nm, 0.08 nm, 0.10 nm, and 0.09 nm, respectively **(Table 3).** Protein segments marked by prominent RMSF spikes delineate zones of amplified structural dynamism; for example, the residue stretch encompassing positions 740–750 in the penfluridol-bound HDAC6 system registered the single largest fluctuation event at 0.78 nm **(Figure 3b).** The extreme fluctuation amplitudes recorded for apo HDAC6, the pimozide-docked complex, and the trichostatin A-docked complex measured 0.57 nm, 0.48 nm, and 0.32 nm, respectively **(Figure 3b)**, (upper panel). Such conformational adaptability entails localized structural rearrangements that might either promote favorable ligand accommodation or fortify the intermolecular contact interface. In marked contrast, residues comprising the trichostatin A-ligated HDAC6 configuration displayed considerably attenuated RMSF responses (~0.32 nm), a hallmark of enhanced conformational restriction, consistent with the stabilized binding mode documented for this complex. The compiled RMSF output, portrayed as a distribution histogram in **Figure 3b**, captures minimally dispersed fluctuation profiles with broadly overlapping patterns sustained longitudinally, corroborating the retention of overall architectural order **(Figure 3b)**, (lower panel).

Compactness analysis

The extent of molecular compaction sustained by each protein–drug conjugate was interrogated via the radius of gyration (Rg) parameter [37]. This observable is instrumental in discerning potential unfolding events or structural distension within the protein matrix during the simulation. An unwavering Rg profile, as consistently observed throughout our computational runs, indicates the absence of appreciable unfolding transitions and confirms the preservation of a stably folded tertiary structure upon ligand complexation. Such behavior is significant for verifying that the binding event does not compromise the global polypeptide fold. The graphical summaries assembled in **Figure 4** illustrate the temporal dependence and the stability–compactness interplay characterizing each complex. The HDAC6–Pimozide trajectory, rendered in green, traces a subtly ascending Rg curve past the 250 ns milestone. The two remaining assemblies—namely HDAC6–Penfluridol and HDAC6–Trichostatin A, depicted in red and blue respectively—nearly coincide with the trace belonging to uncomplexed HDAC6 **(Figure 4a)**. Average Rg quantities derived for the free protein and for the penfluridol-, pimozide-, and trichostatin A-associated states were 1.98 nm, 1.98 nm, 2.00 nm, and 1.98 nm, respectively **(Table 3).** The maximal Rg extents observed for apo HDAC6 and the penfluridol-, pimozide-, and trichostatin A-bound variants reached 2.02 nm, 2.02 nm, 2.04 nm, and 2.03 nm, respectively **(Figure 4a)**, (upper panel). When evaluated jointly, these statistical measures, along with the core Rg evolution plot and the associated probability distribution, collectively argue for persistently well-ordered complex geometry throughout the trajectory **(Figure 4a)**, (lower panel).

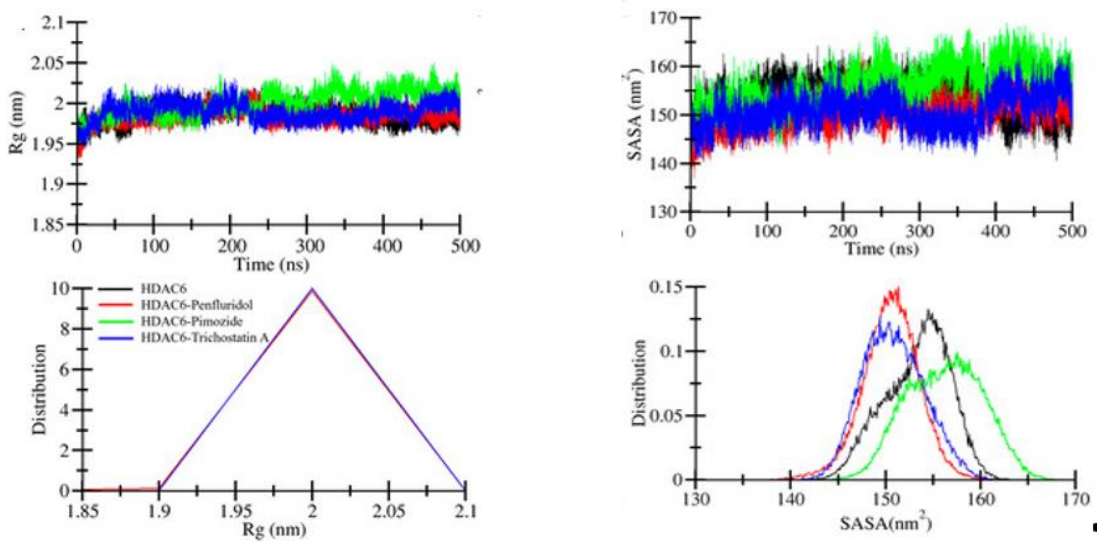

a) b)

Figure 4. Structural compactness assessment plot of (a) Rg of HDAC6, HDAC6-Penfluridol, HDAC6-Pimozide, and HDAC6-Trichostatin A. (b) Solvent-accessible surface area assessment plot of HDAC6, HDAC6-Penfluridol, HDAC6-Pimozide, and HDAC6-Trichostatin A. The lower panels show PDFs of Rg

and SASA distributions. Black, red, green, and blue represent HDAC6, HDAC6-Penfluridol, HDAC6-Pimozide, and HDAC6-Trichostatin A, respectively.

Solvent-accessible surface area (SASA) quantifies the portion of a protein's molecular surface that remains topographically exposed and capable of engaging the surrounding aqueous medium [38]. This descriptor is widely used to track folding–unfolding equilibria within biomolecular constructs, as variations in SASA typically mirror shifts in the extent of solvent exposure of the macromolecule. In the context of this study, average SASA estimates were extracted for free HDAC6 and for its penfluridol-, pimozide-, and trichostatin A-bound counterparts, yielding 153.3 nm², 150.5 nm², 156.2 nm², and 150.8 nm², respectively **(Table 3).** Among the series, the HDAC6–Pimozide conjugate is the sole system exhibiting a modestly expanded solvent-accessible footprint, an effect plausibly rooted in conformational realignments necessitated by ligand docking. Critically, this expansion does not translate into any detectable detriment to the overall protein architecture, as borne out by the SASA graphical output **(Figure 4b).** The extreme SASA values recorded for unliganded HDAC6 and the penfluridol-, pimozide-, and trichostatin A-complexed states were 164.9 nm², 162.8 nm², 168.8 nm², and 163.1 nm², respectively **(Figure 4b)**, (upper panel). The collated numeric data, when inspected together with the principal SASA temporal trace and the related distribution histogram, indicate that the pimozide-bound HDAC6 ensemble experienced a gently sloping upward drift commencing around the 200 ns mark. Yet, no substantial baseline shifts or discontinuous jumps were registered throughout the remainder of the simulation **(Figure 4b)**, (lower panel). In summary, the SASA-derived trends show strong concordance with the Rg-based observations, jointly reinforcing the conclusion that the complexes retain both stability and a compact conformational state.

Hydrogen bond analysis

In biological macromolecular systems, hydrogen bonding is indispensable for maintaining three-dimensional structural organization and conformational stability [39]. To probe the stability of HDAC6 before and after association with the identified compounds, intramolecular hydrogen bond counts were quantified. The mean numbers of internal hydrogen bonds sustained within the protein were 264, 264, 267, and 264 for apo HDAC6 and its penfluridol-, pimozide-, and trichostatin A-bound complexes, respectively **(Table 3)**. The peak intramolecular hydrogen bond tallies recorded for free HDAC6 and the penfluridol-, pimozide-, and trichostatin A-associated forms reached 297, 300, 303, and 295, respectively **(Figure 5).** On balance, the computed outcomes showed that the liganded states formed more internal hydrogen bonds than the unbound protein. The graphical representation provided in **Figure 5a** captures the temporal evolution of hydrogen bond dynamics across the 500 ns trajectory. The frequency distribution histogram further corroborates the elevated bond count exhibited by the HDAC6–Pimozide complex, depicted in green **(Figure 5a).**

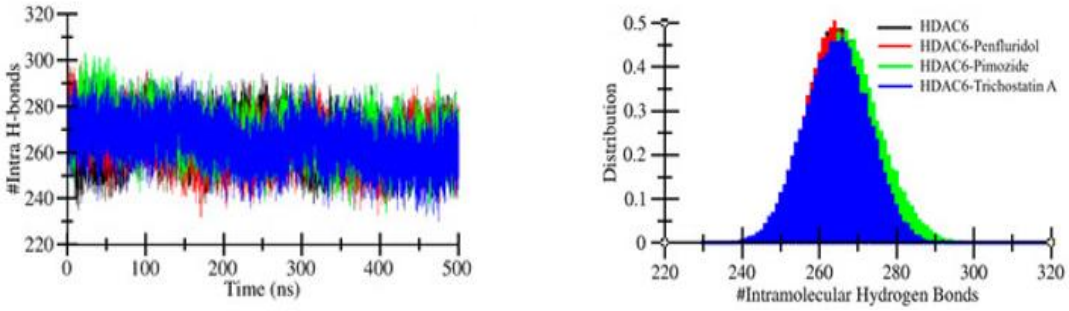

a) b)

Figure 5. Intramolecular hydrogen bonding: (a) Intramolecular hydrogen bond plot of HDAC6 protein before and after interactions of Penfluridol, Pimozide, and Trichostatin A, and (b) Distribution plot of intramolecular hydrogen bonds.

In addition, intermolecular hydrogen bonds at the protein–drug interface were evaluated to clarify further the stability of the assembled complexes [27]. To explore the dynamic behavior and persistence of protein–ligand contacts, we monitored the interactions occurring between HDAC6 and each of the three ligands—penfluridol, pimozide, and trichostatin A—over the entirety of the 500 ns molecular dynamics production phase. The

examination focused on intermolecular hydrogen bonds within the respective protein–ligand constructs. **Figure 6** depicts the maximal numbers of hydrogen bonds detected within the HDAC6–Penfluridol, HDAC6–Pimozide, and HDAC6–Trichostatin A assemblies, which amounted to two, four, and five, respectively. The inspection demonstrated that all three complexes maintained durable contacts with functionally important residues lining the HDAC6-binding cavity. The hydrogen bond count oscillated modestly yet remained broadly consistent throughout; penfluridol maintained an average of 1–2 hydrogen bonds, pimozide maintained 1–2 hydrogen bonds, and trichostatin A consistently displayed 2–3 hydrogen bonds over the simulation duration. A probability distribution plot capturing bonding persistence across the trajectory was constructed for each of the three complexes. A single hydrogen bond within each of the three assemblies occupied a disproportionately larger fraction of the distribution than other contacts, which formed only transiently between protein and drug **(Figure 6**), (lower panels). This sustained contact profile throughout the simulation suggests that the ligands remained securely bound to HDAC6, lending weight to their candidacy as repurposed inhibitory agents.

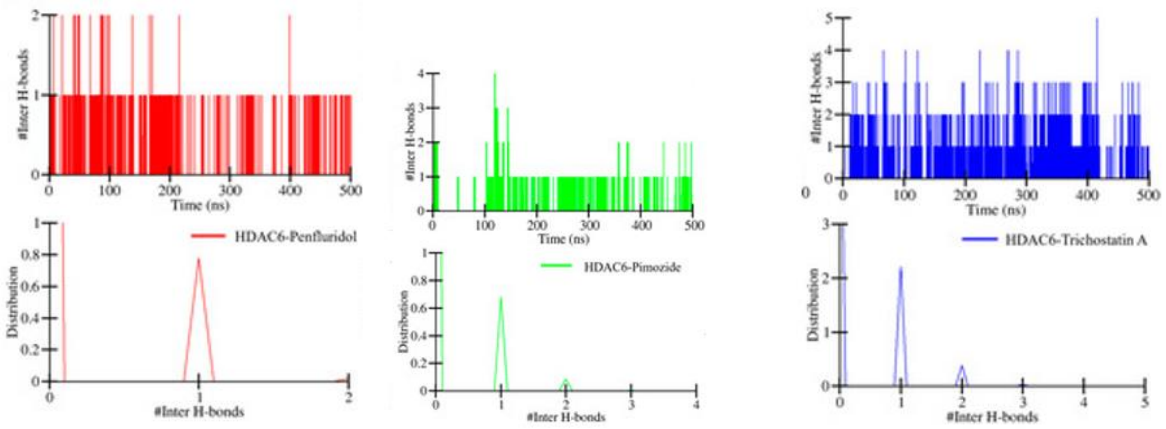

a) b) c)

Figure 6. Intermolecular hydrogen plot of HDAC6–drug complexes. (a) HDAC6-Penfluridol, (b) HDAC6-Pimozide, and (c) HDAC6-Trichostatin A.

Secondary structure alteration analysis

Secondary structure characterization entails tracking modifications across the various elements of the protein's secondary structure, both before and after ligand engagement [28]. This analysis was undertaken to surveil alterations in the protein's secondary structural motifs, including α-helices and β-sheets, over the simulation period. Such monitoring carries significance because pronounced perturbations in secondary structure composition can signal destabilization of the native protein fold upon ligand accommodation. The DSSP algorithm was applied to chart the distribution of secondary structural elements in HDAC6 before and after drug binding. **Figure 7** employs a color-coded scheme to denote structural elements, with black signifying conformations whose residue participation increased over time following drug binding. The HDAC6–Penfluridol, HDAC6–Pimozide, and HDAC6–Trichostatin A complexes each exhibited notable expansions in β-sheet content. Both the pimozide-bound and trichostatin A-bound complexes additionally registered gains in α-helical character.

In contrast, residue involvement in the pimozide-complexed state remained comparable to that of the unliganded protein (Table 4). Throughout this analysis, no substantial remodeling of HDAC6's secondary structure was detected, suggesting that ligand binding does not undermine the protein's architectural integrity. Minor decrements in residue participation within coil regions and β-bridges were noted, likely attributable to conformational accommodations prompted by drug binding. In summary, the secondary structure evaluation predicted no major disruptive alterations across the entire simulation interval, indicating that all complexes remained stably folded.

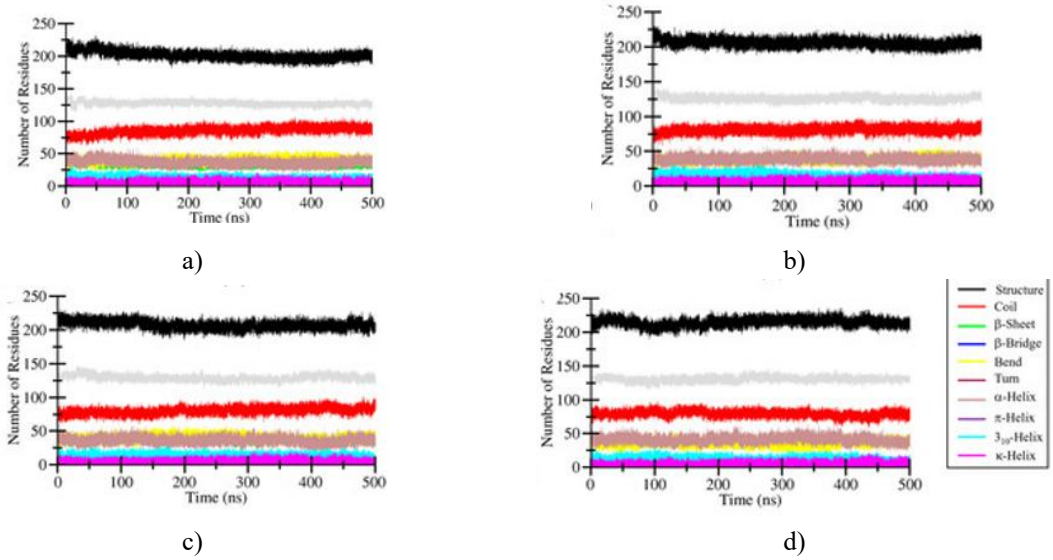

Figure 7. Secondary structure elements representation of (a) HDAC6, (b) HDAC6-Penfluridol, (c) HDAC6-Pimozide, and (d) HDAC6-Trichostatin A.

Table 4. The average number of participating residues in secondary structure elements in HDAC6 during 500 ns MD simulations. Structure = α-Helix + β-sheet + β-Bridge + Turn.

System	PPII-Helix	3_{10}-Helix	π-Helix	α-Helix	Turn	Bend	β-Bridge	β-Sheet	Coil	Total Structure
HDAC6	7 (±3)	14 (±4)	5 (±0)	128 (±3)	37 (±5)	41 (±4)	6 (±2)	31 (±2)	86 (±6)	202 (±6)
HDAC6–Penfluridol	8 (±4)	15 (±4)	5 (±0)	126 (±4)	39 (±4)	37 (±4)	4 (±2)	37 (±1)	81 (±5)	206 (±5)
HDAC6–Pimozide	6 (±3)	14 (±4)	5 (±0)	129 (±4)	37 (±5)	41 (±4)	5 (±2)	37 (±2)	81 (±5)	208 (±6)
HDAC6–Trichostatin A	6 (±3)	13 (±4)	5 (±0)	131 (±4)	42 (±5)	35 (±4)	5 (±1)	37 (±2)	80 (±5)	215 (±6)

Principal component analysis

Principal component analysis (PCA) was performed to extract the dominant modes of collectively correlated atomic motion in HDAC6 and its complexes with the selected drug candidates. This methodology yields a mechanistic understanding of HDAC6's conformational repertoire and structural resilience under distinct ligation states, with emphasis on large-amplitude collective movements frequently linked to functional protein dynamics. PCA was conducted on the 500 ns trajectories of Cα atomic coordinates harvested from the MD simulations of HDAC6 bound to penfluridol, pimozide, and the benchmark ligand trichostatin A **(Figure 8)**. These trajectory datasets were mined to distill the essential dynamical features and concerted motional patterns characterizing each protein–drug assembly. The two principal components (PC1 and PC2), which together account for the largest fraction of variance in the system's atomic coordinate space, were used to decode the principal conformational responses triggered by ligand complexation. In the case of ligand-free HDAC6, the eigenvector projections spanned from −2.28 nm to 3.28 nm along PC1 and from −3.19 nm to 1.65 nm along PC2. Upon association with penfluridol, pimozide, and trichostatin A, the eigenvector boundaries shifted to −3.39 nm to 2.01 nm, −2.76 nm to 1.90 nm, and −2.18 nm to 2.37 nm for PC1, and from −2.25 nm to 2.93 nm, −2.11 nm to 1.89 nm, and −2.22 nm to 1.92 nm for PC2, respectively **(Figure 8a)**. These displacements mirror differential conformational adaptability and stabilization patterns adopted by HDAC6 within each binding context.

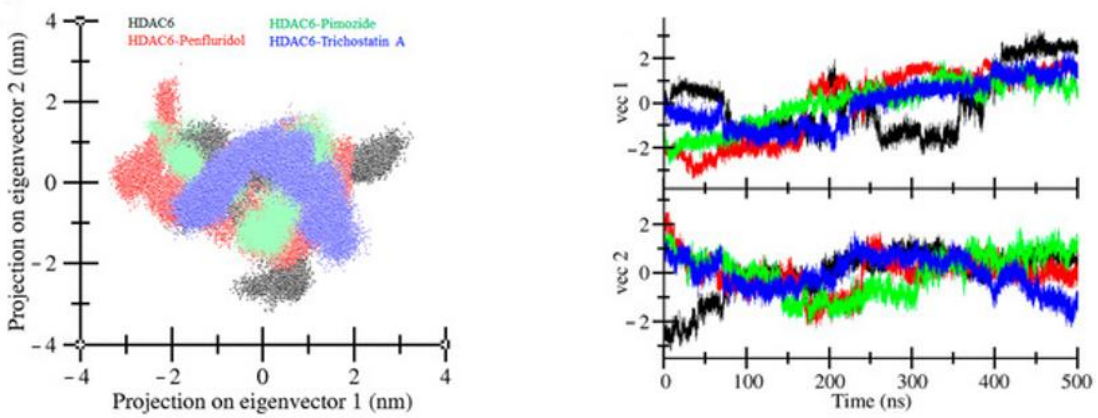

a) b)

Figure 8. Principal component analysis: (a) A 2D projection plot of HDAC6 protein and its complexes with Penfluridol, Pimozide, and Trichostatin A, indicated by different colors, and (b) Time-dependent eigenvector representation of HDAC6 protein and its complexes with Penfluridol, Pimozide, and Trichostatin A, indicated by different colors.

The HDAC6–Penfluridol assembly displayed a moderately broadened distribution along PC2, indicative of increased motional freedom in select loop segments. This finding aligns with the elevated flexibility observed in the preceding RMSF analysis. This conformational latitude may enable penfluridol to maneuver within the binding pocket, thereby potentially augmenting its inhibitory effectiveness. The conformational subspace sampled by the HDAC6–Trichostatin A complex was more constrained than that of the apo reference, suggesting a rigid, well-defined binding mode. This trait may correlate with its high-affinity binding signature. The time-resolved eigenvector trajectory further unveils comparatively dynamic fluctuations in HDAC6 during the simulation, contrasted with a relatively quiescent vector 2 profile across all complexes following an initial 100 ns equilibration phase **(Figure 8b)**. Collectively, the PCA findings in conjunction with the RMSF data indicate that all three ligands enforce stabilized binding-competent conformations of HDAC6. However, penfluridol imparts marginally greater conformational flexibility in the vicinity of loop regions. This supplementary pliability could plausibly contribute to its advantageous binding characteristics and its promise as an HDAC6-directed inhibitor.

Free energy landscapes

Free energy landscapes were derived to map the energetic terrain governing the protein-folding trajectory during the molecular dynamics runs. Contour-level free energy diagrams were constructed for both the apo protein and the drug-bound assemblies, permitting an appraisal of energy distribution that illuminates the underpinnings of stability and the folding itinerary. Within these contour representations, a spectrum of hues—red, yellow, orange, and blue—is used to span the energetic gradient from maxima to minima. The free energy spans for unliganded HDAC6 and its complexes with penfluridol, pimozide, and trichostatin A ranged from 0 to 18 kJ/mol, 0 to 18.8 kJ/mol, 0 to 16.5 kJ/mol, and 0 to 17.3 kJ/mol, respectively **(Figure 9).** The deeply colored blue troughs in the contour plots indicate low-energy basins or regions near zero free energy, demarcating thermodynamically privileged, stable configurations of the polypeptide. In the map corresponding to HDAC6 alone, four such dark blue depressions are discernible, each pointing to a distinct metastable substate **(Figure 9a).** The penfluridol-bound complex is characterized by a single expansive basin flanked by two smaller blue pockets; the pimozide-bound complex, by contrast, features three prominent dark blue depressions supplemented by one minor basin **(Figures 9b and 9c)**. The trichostatin A-associated complex presents a single, large, merged blue basin within which three subsidiary dark blue indentations are nested **(Figure 9d)**. Of particular note, the topographic relief of the penfluridol–HDAC6 contour map appeared noticeably more subdued than that of the remaining landscapes. Viewed holistically, the FEL projections, when interpreted alongside the principal component diagrams, substantiate that each complex successfully descended into its global free energy minimum, thereby exhibiting pronounced stabilization. Synthesizing the body of evidence, the study indicates that both penfluridol and pimozide exhibit promising binding affinity and stability with HDAC6 and further possess acceptable drug-like profiles, supporting their repurposing for neurodegenerative disease management.

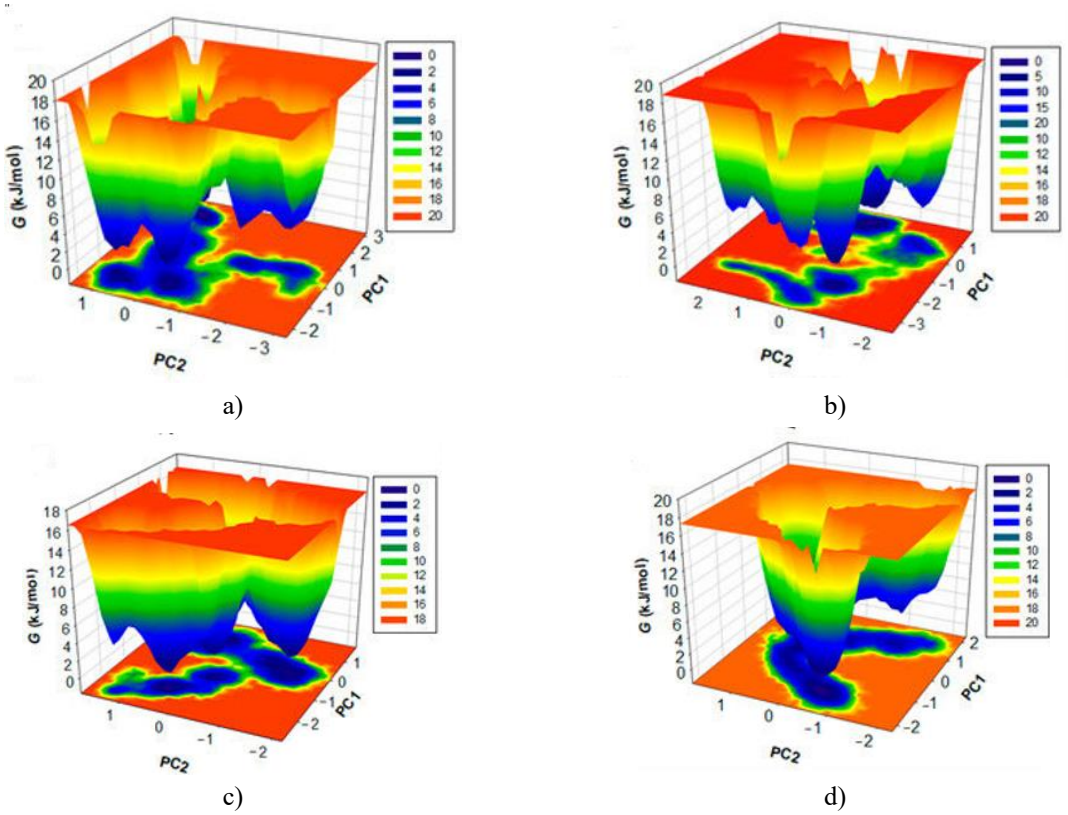

Figure 9. Three-dimensional Gibbs free energy maps of (a) HDAC6, (b) HDAC6-Penfluridol, (c) HDAC6-Pimozide, and (d) HDAC6-Trichostatin A.

MMPBSA analysis

Binding free energy was estimated using the MMPBSA methodology, implemented with the gmx_MMPBSA module in GROMACS, to quantify the energetic signatures of HDAC6–ligand association. This thermodynamic observable encapsulates the net free-energy shift accompanying the formation of the protein–ligand complex, thereby providing a quantitative gauge of interaction potency [40]. The computational protocol resolved the overall binding free energy into its constituent contributions, principally encompassing van der Waals dispersion forces and electrostatic components **(Table 5).** The data confirm that every HDAC6–ligand pairing yields favorable binding free energies, indicative of robust, sustained interactions. Within the panel, HDAC6–Penfluridol showed the most negative binding free energy, positioning it as the system yielding the most thermodynamically stabilized complex.

Table 5. MMPBSA calculations of binding free energy for HDAC6–ligand complexes. All the values are in kcal/mol.

Complex	ΔG_{bind}	ΔG_{sol}	$\Delta G_{nonpolar}$	ΔG_{polar}	ΔG_{gas}	ΔE_{ele}	ΔE_{vdW}
HDAC6-Penfluridol	−52.82	12.08	−6.02	20.66	−48.58	−5.86	−58.60
HDAC6-Pimozide	−56.03	12.82	−4.52	18.52	−50.27	−6.52	−40.12
HDAC6-Trichostatin A	−41.70	6.76	−4.08	10.54	−46.50	−5.90	−46.18

Conclusion

The search for potent and truly effective HDAC6 modulators carries profound implications for the development of next-generation therapeutic regimens for neurodegenerative pathologies. In the work described herein, an integrated computational framework was applied to a collection of 3500 FDA-approved pharmaceuticals, screening them for their potential to interact productively with HDAC6 and regulate its activity. Among the full complement of molecules screened virtually, penfluridol and pimozide emerged as the two most promising repositioning candidates, a distinction rooted in their potent binding properties, drug-likeness profiles, and ability to form persistent, stable interactions with the target enzyme. Extended all-atom molecular dynamics simulations

spanning 500 ns lent further weight to the structural soundness of the resultant protein–ligand adducts, as gauged through an ensemble of diagnostic analyses: structural drift quantification, per-residue motional flexibility, conformational compaction, hydrogen bonding inventory, principal component decomposition, and free energy surface mapping. When interpreted holistically, the body of evidence indicates that penfluridol and pimozide form strong, thermodynamically preferred associations with HDAC6, a conclusion that buttresses the case for their therapeutic redirection toward the clinical management of neurodegenerative disorders. In a complementary vein, MMPBSA energetic profiling revealed consistently negative, and thus favorable, binding free energies across all three HDAC6–ligand partnerships, further cementing the inference that their intermolecular interactions are of a stable character. A necessary caveat remains: the entirety of this study rests upon computational methodologies; accordingly, rigorous wet-laboratory and animal-model validation is imperative before any definitive claims can be made regarding the in vivo pharmacological potency and the safety margins of these compounds. Equally, whilst the simulation component proved adept at assessing the robustness of the formed complexes, it is inherently constrained in its ability to reflect the full gamut of physiological variables and potential untoward reactions. To conclude, the present investigation provides a solid, well-substantiated springboard for subsequent experimental and translational research initiatives. It simultaneously unlocks novel therapeutic possibilities by strategically repurposing these agents to antagonize HDAC6 selectively.

Acknowledgments: The authors acknowledge the generous support from the Research Supporting Project (RSP2024R434) by King Saud University, Riyadh, Kingdom of Saudi Arabia. A.S. is thankful to Ajman University, UAE, for supporting this publication.

Conflict of Interest: None

Financial Support: None

Ethics Statement: None

References

1. Biel M, Wascholowski V, Giannis A. Epigenetics—an epicenter of gene regulation: histones and histone-modifying enzymes. Angew Chem Int Ed. 2005;44:3186-216.
2. Zheng K, Jiang Y, He Z, Kitazato K, Wang Y. Cellular defence or viral assist: the dilemma of HDAC6. J Gen Virol. 2017;98:322-37.
3. Grozinger CM, Hassig CA, Schreiber SL. Three proteins define a class of human histone deacetylases related to yeast Hda1p. Proc Natl Acad Sci U S A. 1999;96:4868-73.
4. Gallinari P, Di Marco S, Jones P, Pallaoro M, Steinkühler C. HDACs, histone deacetylation and gene transcription: from molecular biology to cancer therapeutics. Cell Res. 2007;17:195-211.
5. Yang XJ, Grégoire S. Class II histone deacetylases: from sequence to function, regulation, and clinical implication. Mol Cell Biol. 2005;25:2873-84.
6. Parra M. Class IIa HDACs—new insights into their functions in physiology and pathology. FEBS J. 2015;282:1736-44.
7. Núñez-Álvarez Y, Suelves M. HDAC11: a multifaceted histone deacetylase with proficient fatty deacylase activity and its roles in physiological processes. FEBS J. 2022;289:2771-92.
8. Ciarlo E. Impact of classical and NAD+-dependent (ie sirtuins) histone deacetylases (HDACs) on innate immune responses: lessons from the usage of HDAC inhibitors and sirtuin knockout mice [dissertation]. Lausanne (Switzerland): Université de Lausanne; 2016.
9. Falkenberg KJ, Johnstone RW. Histone deacetylases and their inhibitors in cancer, neurological diseases and immune disorders. Nat Rev Drug Discov. 2014;13:673-91.
10. Zhang XH, Qin-Ma, Wu HP, Khamis MY, Li YH, Ma LY, et al. A review of progress in histone deacetylase 6 inhibitors research: structural specificity and functional diversity. J Med Chem. 2021;64:1362-91.
11. Zhu Y, Feng M, Wang B, Zheng Y, Jiang D, Zhao L, et al. New insights into the non-enzymatic function of HDAC6. Biomed Pharmacother. 2023;161:114438.

12. Van Helleputte L, Benoy V, Van Den Bosch L. The role of histone deacetylase 6 (HDAC6) in neurodegeneration. Res Rep Biol. 2014;5:1-13.
13. Simões-Pires C, Zwick V, Nurisso A, Schenker E, Carrupt PA, Cuendet M. HDAC6 as a target for neurodegenerative diseases: what makes it different from the other HDACs? Mol Neurodegener. 2013;8:7.
14. Shen S, Kozikowski AP. A patent review of histone deacetylase 6 inhibitors in neurodegenerative diseases (2014-2019). Expert Opin Ther Pat. 2020;30:121-36.
15. Parvathaneni V, Kulkarni NS, Muth A, Gupta V. Drug repurposing: a promising tool to accelerate the drug discovery process. Drug Discov Today. 2019;24:2076-85.
16. Park K. A review of computational drug repurposing. Transl Clin Pharmacol. 2019;27:59-63.
17. Daśko M, de Pascual-Teresa B, Ortín I, Ramos A. HDAC inhibitors: innovative strategies for their design and applications. Molecules. 2022;27:715.
18. Knox C, Wilson M, Klinger CM, Franklin M, Oler E, Wilson A, et al. DrugBank 6.0: the DrugBank knowledgebase for 2024. Nucleic Acids Res. 2024;52:D1265-75.
19. Huey R, Morris GM, Forli S. Using AutoDock 4 and AutoDock Vina with AutoDockTools: a tutorial. La Jolla (CA): Scripps Research Institute; 2012.
20. Mohammad T, Mathur Y, Hassan MI. InstaDock: a single-click graphical user interface for molecular docking-based virtual high-throughput screening. Brief Bioinform. 2021;22:bbaa279.
21. DeLano WL. PyMOL: an open-source molecular graphics tool. CCP4 Newsl Protein Crystallogr. 2002;40:82-92.
22. Discovery Studio Visualizer. Version 2.0. San Diego (CA): Accelrys Software Inc.; 2005.
23. Filimonov D, Lagunin A, Gloriozova T, Rudik A, Druzhilovskii D, Pogodin P, et al. Prediction of the biological activity spectra of organic compounds using the PASS online web resource. Chem Heterocycl Compd. 2014;50:444-57.
24. Shamsi A, Khan MS, Altwaijry N, Hassan N, Shahwan M, Yadav DK. Targeting PDE4A for therapeutic potential: exploiting drug repurposing approach through virtual screening and molecular dynamics. J Biomol Struct Dyn. 2024:1-13.
25. Huang J, MacKerell AD Jr. CHARMM36 all-atom additive protein force field: validation based on comparison to NMR data. J Comput Chem. 2013;34:2135-45.
26. Mark P, Nilsson L. Structure and dynamics of the TIP3P, SPC, and SPC/E water models at 298 K. J Phys Chem A. 2001;105:9954-60.
27. Van Der Spoel D, Lindahl E, Hess B, Groenhof G, Mark AE, Berendsen HJC. GROMACS: fast, flexible, and free. J Comput Chem. 2005;26:1701-18.
28. Zhu S. Validation of the generalized force fields GAFF, CGenFF, OPLS-AA, and PRODRGFF by testing against experimental osmotic coefficient data for small drug-like molecules. J Chem Inf Model. 2019;59:4239-47.
29. Gorelov S, Titov A, Tolicheva O, Konevega A, Shvetsov A. DSSP in Gromacs: tool for defining secondary structures of proteins in trajectories. J Chem Inf Model. 2024;64:3593-8.
30. Sittel F, Jain A, Stock G. Principal component analysis of molecular dynamics: on the use of Cartesian vs. internal coordinates. J Chem Phys. 2014;141:014111.
31. Papaleo E, Mereghetti P, Fantucci P, Grandori R, De Gioia L. Free-energy landscape, principal component analysis, and structural clustering to identify representative conformations from molecular dynamics simulations: the myoglobin case. J Mol Graph Model. 2009;27:889-99.
32. Genheden S, Ryde U. The MM/PBSA and MM/GBSA methods to estimate ligand-binding affinities. Expert Opin Drug Discov. 2015;10:449-61.
33. Shamsi A, Mohammad T, Khan MS, Shahwan M, Husain FM, Rehman MT, et al. Unraveling binding mechanism of Alzheimer's drug rivastigmine tartrate with human transferrin: molecular docking and multi-spectroscopic approach towards neurodegenerative diseases. Biomolecules. 2019;9:495.
34. Mannhold R, Kubinyi H, Folkers G. Protein-ligand interactions: from molecular recognition to drug design. Hoboken (NJ): John Wiley & Sons; 2006.
35. Naqvi AA, Mohammad T, Hasan GM, Hassan MI. Advancements in docking and molecular dynamics simulations towards ligand-receptor interactions and structure-function relationships. Curr Top Med Chem. 2018;18:1755-68.

36. Maiorov VN, Crippen GM. Significance of root-mean-square deviation in comparing three-dimensional structures of globular proteins. J Mol Biol. 1994;235:625-34.
37. Lobanov MY, Bogatyreva N, Galzitskaya OV. Radius of gyration as an indicator of protein structure compactness. Mol Biol. 2008;42:623-8.
38. Martins JM, Ramos RM, Pimenta AC, Moreira IS. Solvent-accessible surface area: how well can be applied to hot-spot detection? Proteins. 2014;82:479-90.
39. Hubbard RE, Haider MK. Hydrogen bonds in proteins: role and strength. eLS. 2010:1-6.
40. Wang E, Sun H, Wang J, Wang Z, Liu H, Zhang JZ, et al. End-point binding free energy calculation with MM/PBSA and MM/GBSA: strategies and applications in drug design. Chem Rev. 2019;119:9478-508.